JOURNAL OF AIRCRAFT
Vol. 54, No. 2, March–April 2017

Concurrent Active Piezoelectric Control and Energy Harvesting of Highly Flexible Multifunctional Wings

Natsuki Tsushima* and Weihua Su†
University of Alabama, Tuscaloosa, Alabama 35487-0280

DOI: 10.2514/1.C033846

Both active actuation and energy harvesting of highly flexible wings using piezoelectric transduction are studied in this paper. The piezoelectric effect is included in a strain-based geometrically nonlinear beam formulation. The resulting structural dynamic equations for multifunctional beams are then coupled with a finite-state unsteady aerodynamic formulation, allowing for piezoelectric energy harvesting and actuation with the nonlinear aeroelastic system. With the development, it is possible to provide an integral aeroelastic and electromechanical solution of concurrent active piezoelectric control and energy harvesting for wing vibrations, with the consideration of the geometrical nonlinear effects of slender multifunctional wings. In this paper, linear quadratic regulator and linear quadratic Gaussian controllers are developed for the active control of wing vibrations. The controllers demonstrate effective gust alleviation capabilities. Furthermore, concurrent active vibration control and energy harvesting can also be realized for the multifunctional wings with embedded piezoelectric materials. From this numerical study, the impact of the piezoelectric actuator and energy harvester placement on wing performance is benchmarked.

Nomenclature

$\boldsymbol{A}$	=	system matrix in state-space equation
A	=	cross-section area of piezoelectric layer, m^2
a_0	=	local aerodynamic frame, with a_{0x} axis pointing to wing tip and a_{0y} axis aligned with zero lift line of airfoil
a_1	=	local aerodynamic frame, with a_{1y} axis aligned with airfoil motion velocity
B	=	body reference frame
$\boldsymbol{B}$	=	control matrix in state-space equation
$\boldsymbol{B}_{vh}$, $\boldsymbol{B}_{va}$	=	piezoelectric coupling matrix for harvester and actuator
B_{vh}^{cs}	=	cross-sectional piezoelectric coupling matrix
$\bar{\boldsymbol{B}}$	=	electric displacement, C/m^2
$\boldsymbol{B}^F$, $\boldsymbol{B}^M$	=	influence matrices for distributed forces and moments
b_c	=	semichord of airfoil, m
b_p	=	chordwise width of piezoelectric layer, m
$\boldsymbol{C}$	=	coefficient matrix for state vector in state-space output model
C_p	=	capacitance of energy harvesting system, F
$\boldsymbol{D}$	=	coefficient matrix for control input in state-space output model
$\bar{\boldsymbol{D}}$	=	piezoelectric material stiffness matrix
d	=	distance of midchord in front of beam reference axis, m
$\boldsymbol{E}$	=	electric field, V/m
$\boldsymbol{e}$	=	piezoelectric coupling, C/m^2
e_{31}	=	transverse piezoelectric coupling, C/m^2
e_{36}	=	piezoelectric coupling for induced shear stress, C/m^2
$\boldsymbol{F}_i$	=	influence matrices in inflow equations with independent variables (with i equal to 1, 2, and 3)
F_{ia}, M_{ia}	=	piezoelectric induced force and moment in beam coordinate (with i equal to 1, 2, and 3)
$\boldsymbol{F}^{\text{dist}}$, $\boldsymbol{F}^{\text{pt}}$	=	distributed and point forces
$\boldsymbol{G}$	=	coefficient matrix for disturbance (process noise) in state-space system model
$\boldsymbol{g}$	=	gravity acceleration column vector, m/s^2
$\boldsymbol{H}$	=	coefficient matrix for disturbance (process noise) in state-space output model
$\boldsymbol{h}$	=	absolute positions and orientations of beam nodes
i	=	electric current in circuit of energy harvesting system, A
J, J_s, J_c	=	total system, state, and control cost functions
$\boldsymbol{J}_{he}$, $\boldsymbol{J}_{pe}$, $\boldsymbol{J}_{\theta e}$	=	Jacobian matrix
$\boldsymbol{K}$	=	control gain
l_{mc}, m_{mc}, d_{mc}	=	aerodynamic lift, moment, and drag on airfoil about its midchord
$\boldsymbol{M}_{FF}$, $\boldsymbol{C}_{FF}$, $\boldsymbol{K}_{FF}$	=	generalized inertia, damping, and stiffness matrices
$\bar{\boldsymbol{M}}_{FF}$, $\bar{\boldsymbol{C}}_{FF}$, $\bar{\boldsymbol{K}}_{FF}$	=	linearized generalized inertia, damping, and stiffness matrices
$\boldsymbol{M}_s$, $\boldsymbol{C}_s$, $\boldsymbol{K}_s$	=	discrete inertia, damping, and stiffness matrices of whole system
$\boldsymbol{M}^{\text{dist}}$, $\boldsymbol{M}^{\text{pt}}$	=	distributed and point moments
$\boldsymbol{N}$	=	influence matrix for gravity force
$\boldsymbol{n}$	=	sensor noise
$\boldsymbol{p}_w$	=	position of w frame resolved in B frame
$\boldsymbol{Q}$, $\boldsymbol{R}$	=	penalty matrix for control input and state vector
Q_e	=	total charge accumulated over electrodes, C
R_e	=	resistance of energy harvesting circuit, Ω
R_F	=	components of generalized load vector
$\boldsymbol{R}_{F/\lambda_0}^{\text{aero}}$	=	derivative of aerodynamic load vector with respect to inflow states
r	=	weighting parameter of control penalties
s	=	beam curvilinear coordinate, m
s_p	=	spanwise length of piezoelectric layer, m
T_s, T_e	=	transformation matrices of composites
t_p	=	thickness of piezoelectric layer, m
U_∞	=	aircraft trim velocity or freestream velocity, m/s
$\boldsymbol{u}$	=	control input to system plant

Presented as Paper 2016-0715 at the 57th AIAA/ASCE/AHS/ASC Structures, Structural Dynamics, and Materials Conference, San Diego, CA, 04–08 January 2016; received 25 December 2015; revision received 4 July 2016; accepted for publication 5 July 2016; published online 3 October 2016.

*Ph.D. Student, Department of Aerospace Engineering and Mechanics; ntsushima@crimson.ua.edu. Student Member AIAA.

†Assistant Professor, Department of Aerospace Engineering and Mechanics; suw@eng.ua.edu. Senior Member AIAA.

v	=	voltage of multifunctional system, V
W^{ext}, W^{int}	=	external and internal virtual work
$\boldsymbol{w}$	=	disturbance to system (process noise)
w	=	local beam frame resolved in B frame
$\boldsymbol{x}$	=	state vector of system plant
$\hat{\boldsymbol{x}}$	=	state vector estimate of system plant
$\boldsymbol{y}$	=	output vector of system plant
$\dot{y}$, $\dot{z}$	=	airfoil translational velocity components resolved in local aerodynamic frame, m/s
z_p	=	distance between elastic axis of beam and piezoelectric layer, m
$\dot{\alpha}$	=	airfoil angular velocity about a_{0x} axis, rad/s
$\boldsymbol{\varepsilon}$	=	total beam strain vector
$\boldsymbol{\varepsilon}_x$	=	extensional strain in beam members
$\boldsymbol{\varepsilon}_0$	=	initial beam strain vector
$\bar{\boldsymbol{\varepsilon}}$	=	material strain in piezoelectric constitutive relation
ζ	=	permittivity, F/m
$\boldsymbol{\theta}$	=	rotations of beam nodes, rad
κ_x, κ_y, κ_z	=	torsional, flat bending, and edge bending rates of beam members, 1/m
$\boldsymbol{\lambda}$	=	inflow states, m/s
λ_0	=	inflow velocities, m/s
ρ	=	air density, kg/m$_3$
$\bar{\boldsymbol{\sigma}}$	=	material stress in piezoelectric constitutive relation, Pa
1, 2, 3	=	beam coordinate in composite material

Subscripts

eq	=	reference nonlinear equilibrium state in which linearization is performed
$h\varepsilon$	=	$\boldsymbol{h}$ vector with respect to strain
$p\varepsilon$	=	nodal position $\boldsymbol{p}_w$ with respect to strain $\boldsymbol{\varepsilon}$
$\theta\varepsilon$	=	nodal rotation $\boldsymbol{\theta}$ with respect to strain $\boldsymbol{\varepsilon}$

I. Introduction

UNMANNED aerial vehicles (UAVs) have been developed for different applications for several years. For example, the U.S. Air Force has been working on a new generation of intelligence, surveillance, and reconnaissance platform called Sensorcraft [1]. On the other hand, NASA initiated the Environmental Research Aircraft and Sensor Technology program, the aim of which was to develop UAVs capable of very high-altitude and long-endurance flights for atmospheric research purposes. Under this program, an evolutionary series of unmanned aircraft (Pathfinder, Pathfinder-Plus, Centurion, and Helios Prototype) was developed by AeroVironment, Inc. These high-altitude long-endurance (HALE) aircraft feature high-aspect-ratio slender wings with a low structural weight fraction. The slender wings may undergo large deformations under normal operation conditions, exhibiting geometrically nonlinear behaviors [2–5]. Therefore, geometrical nonlinearity must be properly taken into account in the aeroelastic modeling of highly flexible vehicles [2,3,6–8].

Meanwhile, different techniques have been developed and applied to improve the aircraft performance and to facilitate the long-endurance flight, of which wing morphing has become a dynamic research topic. The technique is hoped to improve the flight performance under different flight conditions, in which traditional control surfaces are less effective. It may also be possible to provide extra control authority in poor flight conditions. An early concept of wing warping was employed in the aircraft built by the Wright brothers, which was later replaced by discrete control surfaces due to the lack of the structural stiffness. In recent studies of the active aeroelastic wing (AAW) [9,10], a set of control surfaces was used to produce the favorable wing aeroelastic deformation so as to improve the aircraft flight performance, instead of directly generating the maneuver loads. The studies showed promising benefits of the AAW technology in weight, drag, and control performance perspectives. However, for better performance of morphing wings, one needs to apply the proper actuation mechanism and scheme, with sufficient energy to drive the mechanism.

Additionally, multifunctional structural technologies [11] are being developed, which may bring revolutionary changes to aircraft structures. These structures are capable of performing multiple primary functions and can potentially improve the aircraft performance through consolidation of subsystem materials and functions [11,12]. The employment of the wing morphing concept and multifunctional structural technologies may create new aircraft platforms with enhanced effectiveness and improved capability of operation. Active materials, such as anisotropic piezocomposite actuators [13,14], may be used to build multifunctional structures. In fact, one may take advantage of piezoelectric transducers to fulfill the dual functions of both actuation and energy harvesting [15]. Actually, for HALE aircraft in which energy usually constrains their flight range and endurance, the extra energy can be accumulated from the ambient with different mechanisms, such as the piezoelectric effect [16], thermoelectric effect [17], pyroelectric effect, photovoltaic effect, magnetostatic effect, etc. Among them, mechanical vibrations of structural components have been considered as a major energy source [18], with piezoelectric materials embedded into wing structures as sensors and harvesters. This is essentially an inversed application of the piezoelectric effect involved in the wing actuation. To explore the approaches to model the electromechanical behavior of piezoelectric transducing, many research groups from different fields have developed various prediction models. Early studies of piezoelectric transducing have modeled the piezoelectric transducer using a simplified lumped model with bending vibrations [19,20]. Even though the approach was effective, the lumped model came with some disadvantages, such as the oversimplification of the real physics. To improve the accuracy, some distributed models have been applied in the subsequent studies. For example, Bilgen et al. [21] modeled the cantilever beam with embedded piezoelectric materials using the linear Euler–Bernoulli beam theory and applied this approach to the piezoelectric transducing and gust alleviation of a small UAV [22]. Sodano et al. [23] developed a model of the piezoelectric power harvesting device based on the works of Hagood et al. [24] and Crawley and Anderson [25]. They used energy methods to develop the constitutive equations of a bimorph piezoelectric cantilever beam. The model was solved with the Rayleigh–Ritz procedure. Erturk and Inman [26] provided corrections and necessary clarifications for physical assumptions in piezoelectric transducing. More recently, Anton et al. [12] presented the investigation of a multifunctional wing spar for small UAVs.

On the other hand, the piezoelectric actuation was implemented for aerospace applications in many ways. For example, Bent et al. [27] developed the actuator equations for piezoelectric fiber composites with a conventional poling condition. They applied the Classical Laminated Plate Theory for the anisotropic composites force calculations. Wilkie et al. [28] employed this approach to find the piezoelectric induced stress and to calculate the resultant moment on a rectangular, thin-walled, closed-section structure with the piezoelectric twist actuation. Cesnik and Ortega-Morales [29] used an energy approach to develop the actuation equations for a composite wing. They compared their model capability with preceding studies in the literature [30,31].

From the discussion, it can be seen that piezoelectric materials have successfully been integrated in aircraft structures as energy harvesters or actuators in the previous work. However, the study can be advanced regarding how to actively and concurrently take advantage of both functions of piezoelectric transduction in an integral wing structure. Such an integral structure may work with one or both of the two functions of piezoelectric transduction, which can be either actuated for wing morphing and/or vibration control, replacing the traditional control surfaces, or used as an energy harvester, depending on the flight condition and mission. If such a multifunctional wing is designed to be adaptive to the flight conditions, the dual functions of the wing may help to improve the aircraft flight performance by actively controlling the wing vibration and/or providing additional power from the harvested energy. Therefore, it is of interest to understand how such a multifunctional

wing may adaptively improve the aircraft flight performance under different flight conditions.

Furthermore, in the current study on multifunctional wings of HALE aircraft, the piezoelectric energy harvesting and actuation need to be properly modeled in a suitable aeroelastic framework for the highly flexible wings, with the consideration of the aforementioned geometrically nonlinear effects. The traditional approach of modeling the piezoelectric energy harvesting using a linear beam theory are not suitable. In a previous work [32], the authors modeled the piezoelectric energy harvesting of a highly flexible wing, using a strain-based geometrically nonlinear aeroelastic formulation. The advantages of the strain-based geometrically nonlinear beam formulation in the studies of highly flexible structures have been discussed by Su and Cesnik [33]. In the current work, the piezoelectric actuation will be concurrently modeled with the piezoelectric energy harvesting in the nonlinear aeroelastic formulation, which enables the exploration of the aeroelastic and control characteristics of such highly flexible dual-functional wings. To carry out such studies, control algorithms are also required to properly actuate the active wings to achieve the desired aircraft performance. In a modern aircraft control system, there are multiple variables that need to be controlled simultaneously. To satisfy the mission requirement and achieve the desired flight performance, an optimal feedback strategy should be implemented. In a simple control problem, a linear quadratic regulator (LQR) or more practical linear quadratic Gaussian (LQG) regulator may be selected as the starting point. These regulators are popular due to their capability to obtain the optimal control configurations. Several works [34–36] have provided detailed discussions on these controllers.

In summary, this paper will model both active piezoelectric actuation and energy harvesting in a strain-based geometrically nonlinear aeroelastic formulation. This new development will allow for the study of integral piezoelectric actuation and energy harvesting of the multifunctional structure, with the consideration of the geometrically nonlinear aeroelastic effect. Numerical studies will be performed to explore the concurrent piezoelectric energy harvesting and wing vibration control of such a highly flexible multifunctional wing with external gust perturbations. Specifically, the impact of the piezoelectric actuator and energy harvester placement on the wing performance will be benchmarked in this paper. This study lays ground for the further optimal design of the onboard piezoelectric devices and the control settings of the multifunction wing.

II. Theoretical Formulation

The theoretical formulation used in the current study is introduced in this section, where a slender wing with piezoelectric actuation is modeled using a strain-based geometrically nonlinear beam formulation. The strain-based beam [33] and aeroelastic [4,5] formulations have been introduced in the literature. The finite-state inflow theory [37] is incorporated for aerodynamic loads on lifting surfaces. Piezoelectric actuation is considered as an additional external load to the system.

A. Multifunctional Wing Structure

Figure 1 illustrates a multifunctional beam with both energy harvesting and actuation capabilities, using piezoelectric materials. The current work is an extension to the piezoelectric actuation based on the previous work on the modeling of the piezoelectric energy harvesting [32]. For simplicity, the piezoelectric energy harvesting work in the out-of-plane (flat) bending direction. It is sometimes called the transverse piezoelectric effects (3–1 effects). The actuator and the harvester are controlled by a controller on a printed circuit board (PCB), even though the design of a PCB is not discussed in this paper.

The constitutive equation for piezoelectric materials is given as

$$\begin{Bmatrix} \bar{\boldsymbol{\sigma}} \\ \bar{\boldsymbol{B}} \end{Bmatrix} = \begin{bmatrix} \bar{\boldsymbol{D}} & -\boldsymbol{e}^T \\ \boldsymbol{e} & \boldsymbol{\zeta} \end{bmatrix} \begin{Bmatrix} \bar{\boldsymbol{\varepsilon}} \\ \boldsymbol{E} \end{Bmatrix} \tag{1}$$

where $\bar{\boldsymbol{\sigma}}$ is the material stress, $\bar{\boldsymbol{B}}$ is the electric displacement, $\bar{\boldsymbol{D}}$ is the piezoelectric material stiffness matrix, $\boldsymbol{e}$ is the piezoelectric coupling, $\boldsymbol{\zeta}$ is the permittivity, $\bar{\boldsymbol{\varepsilon}}$ is the material strain, and $\boldsymbol{E}$ is the electric field, which is obtained from the gradient of the electric voltage v across the piezoelectric layer:

$$\boldsymbol{E} = \begin{Bmatrix} E_x \\ E_y \\ E_z \end{Bmatrix} = \begin{Bmatrix} -v_{,x} \\ -v_{,y} \\ -v_{,z} \end{Bmatrix} \tag{2}$$

The coupled electromechanical effect of piezoelectric material will be considered when deriving the equations of motion.

B. Fundamental Descriptions of Beam Model

A cantilever beam is defined in a fixed frame B. A local beam frame w is built within the B frame (see Fig. 2), which is used to define the position and orientation of each node along the beam reference line. Vectors $\boldsymbol{w}_x(s,t)$, $\boldsymbol{w}_y(s,t)$, and $\boldsymbol{w}_z(s,t)$ are bases of the beam frame w, the directions of which are pointing along the beam reference axis, toward the leading edge, and normal to the beam (wing) surface, respectively, resolved in the B frame. The curvilinear beam coordinate s provides the nodal location within the body frame.

To model the elastic deformation of slender beams, a nonlinear beam element was developed in the work of Ref. [33]. Each of the elements has three nodes and four local strain degrees of freedom, which are the extension, twist, flat bending rate (κ_y), and edge bending rate (κ_z), respectively, of the beam reference line,

$$\boldsymbol{\varepsilon}^T(s) = \{\, \varepsilon_x(s) \quad \kappa_x(s) \quad \kappa_y(s) \quad \kappa_z(s) \,\} \tag{3}$$

which is not to be confused with the strain of the materials ($\bar{\boldsymbol{\varepsilon}}$) in Eq. (1), even though they are related.

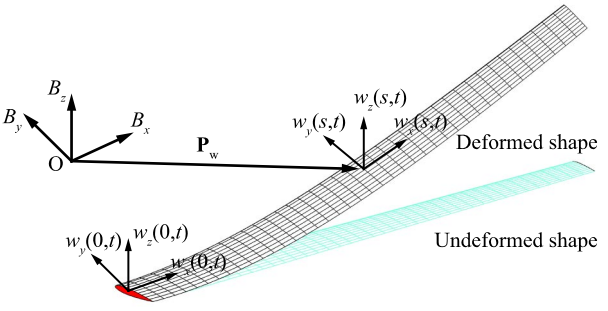

Fig. 2 Beam references frames.

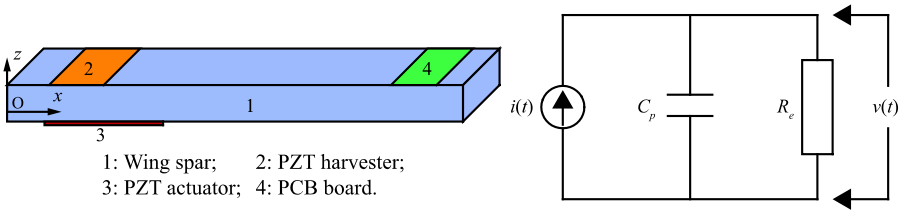

1: Wing spar; 2: PZT harvester;
3: PZT actuator; 4: PCB board.

Fig. 1 (Left) multifunctional wing spar. (Right) equivalent circuit for energy harvesting subsystem (PZT, piezoelectric material).

Positions and orientations of each node along the beam are determined by a vector consisting of 12 components, which is denoted as

$$\boldsymbol{h}^T(s) = \left\{ \boldsymbol{p}_w^T(s) \quad \boldsymbol{w}_x^T(s) \quad \boldsymbol{w}_y^T(s) \quad \boldsymbol{w}_z^T(s) \right\}^T \tag{4}$$

where $\boldsymbol{p}_w$ is the nodal position resolved in the B frame and the orientation is represented by the base vectors of the w frame ($\boldsymbol{w}_x$, $\boldsymbol{w}_y$, and $\boldsymbol{w}_z$). The derivative and variation-dependent variable $\boldsymbol{h}$ are derived from those of the independent variable $\boldsymbol{\varepsilon}$ using the Jacobians, given as

$$\delta\boldsymbol{h} = \boldsymbol{J}_{h\varepsilon}\delta\boldsymbol{\varepsilon} \quad d\boldsymbol{h} = \boldsymbol{J}_{h\varepsilon}d\boldsymbol{\varepsilon} \quad \dot{\boldsymbol{h}} = \boldsymbol{J}_{h\varepsilon}\dot{\boldsymbol{\varepsilon}} \quad \ddot{\boldsymbol{h}} = \boldsymbol{J}_{h\varepsilon}\ddot{\boldsymbol{\varepsilon}} + \dot{\boldsymbol{J}}_{h\varepsilon}\dot{\boldsymbol{\varepsilon}} \tag{5}$$

where the Jacobians are obtained from kinematics [6,33],

$$\boldsymbol{J}_{h\varepsilon} = \frac{\partial \boldsymbol{h}}{\partial \boldsymbol{\varepsilon}} \quad \boldsymbol{J}_{p\varepsilon} = \frac{\partial \boldsymbol{p}_w}{\partial \boldsymbol{\varepsilon}} \quad \boldsymbol{J}_{\theta\varepsilon} = \frac{\partial \boldsymbol{\theta}}{\partial \boldsymbol{\varepsilon}} \tag{6}$$

with $\boldsymbol{J}_{p\varepsilon}$ and $\boldsymbol{J}_{\theta\varepsilon}$ being additional Jacobians relating the nodal position and orientation to the elemental strain [6,33].

C. Equations of Motion

The equations of motion can be derived by following the principle of virtual work extended to dynamic systems, which is equivalent to Hamilton's Principle. The detailed derivation, where the electromechanical coupling effect was not considered, can be found in previous works of the Su and Cesnik [4,33]. The electromechanical coupling effect was further discussed and studied for energy harvesting [32]. The internal virtual work will include contributions of inertia forces, internal strains, strain rates, and the electromechanical effects,

$$\begin{aligned}\delta W^{\text{int}} = &-\delta\boldsymbol{h}^T\boldsymbol{M}_s\ddot{\boldsymbol{h}} - \delta\boldsymbol{\varepsilon}^T\boldsymbol{C}_s\dot{\boldsymbol{\varepsilon}} - \delta\boldsymbol{\varepsilon}^T\boldsymbol{K}_s(\boldsymbol{\varepsilon} - \boldsymbol{\varepsilon}_0) \\ &+ \delta\boldsymbol{\varepsilon}^T(\boldsymbol{B}_{va} + \boldsymbol{B}_{vh})v + \delta v(\boldsymbol{B}_{vh}^T\boldsymbol{\varepsilon} + C_p v)\end{aligned} \tag{7}$$

where $\boldsymbol{\varepsilon}_0$ is the initial strain of the beam. $\boldsymbol{B}_{va}$ and $\boldsymbol{B}_{vh}$ are the electromechanical coupling matrix for the piezoelectric actuator and harvester, respectively. The coupling matrix $\boldsymbol{B}_{va}$ will be derived in the succeeding discussion, while $\boldsymbol{B}_{vh}$ is obtained from the cross-sectional value,

$$\begin{aligned}\boldsymbol{B}_{vh} &= [0 \quad 0 \quad B_{vh} \quad 0]^T \\ B_{vh} &= B_{vh}^{\text{cs}}\, s_p = s_p \int_A -\frac{z_p e_{31}}{t_p}\, \mathrm{d}A\end{aligned} \tag{8}$$

where A is the cross-sectional area of the piezoelectric layer. The distance between the elastic axis of the beam and the piezoelectric layer is z_p (see Fig. 3 for example). Quantities b_p, t_p, and s_p are the width, thickness, and length of the piezoelectric layer, respectively. The capacitance of the energy harvester is defined as

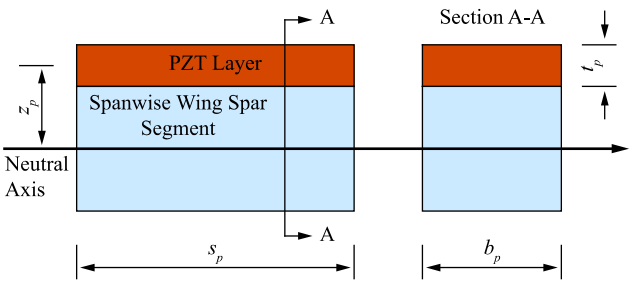

Fig. 3 Spanwise segment and cross-section of multifunctional wing spar (PZT, piezoelectric material).

$$C_p = \zeta\frac{b_p s_p}{t_p} \tag{9}$$

Note that when the bimorph structure connecting piezoelectric layers in parallel is considered the electromechanical coupling and capacitance will be doubled. The external work includes contributions of gravitational force, distributed force, distributed moment, point force, point moment, and the work of the electric charge of the piezoelectric layer. The total external virtual work is

$$\begin{aligned}\delta W^{\text{ext}} = &\delta\boldsymbol{h}^T\boldsymbol{N}\boldsymbol{g} + \delta\boldsymbol{p}_w^T\boldsymbol{B}^F\boldsymbol{F}^{\text{dist}} + \delta\boldsymbol{\theta}^T\boldsymbol{B}^M\boldsymbol{M}^{\text{dist}} + \delta\boldsymbol{p}_w^T\boldsymbol{F}^{\text{pt}} \\ &+ \delta\boldsymbol{\theta}^T\boldsymbol{M}^{\text{pt}} + \delta v Q_e\end{aligned} \tag{10}$$

where $\boldsymbol{g}$, $\boldsymbol{F}^{\text{dist}}$, $\boldsymbol{M}^{\text{dist}}$, $\boldsymbol{F}^{\text{pt}}$, and $\boldsymbol{M}^{\text{pt}}$ are the gravity field, distributed forces, distributed moments, point forces, and point moments, respectively. $\boldsymbol{N}$, $\boldsymbol{B}^F$, and $\boldsymbol{B}^M$ are the influence matrices for the gravitational force, distributed forces, and distributed moments, which come from the numerical integration. In addition, Q_e is the total charge accumulated over the electrodes, the time derivative of which is the current:

$$\frac{\mathrm{d}Q_e}{\mathrm{d}t} = i = \frac{v}{R_e} \tag{11}$$

Based on Eqs. (7) and (10), the variations of the dependent variables ($\boldsymbol{h}$, $\boldsymbol{p}_w$, and $\boldsymbol{\theta}$) and their time derivatives can be replaced by the independent variable $\boldsymbol{\varepsilon}$ by applying the Jacobians [see Eq. (5)] and their subsets. Therefore, the total virtual work on a beam can be written as

$$\begin{aligned}\delta W = &-\delta\boldsymbol{\varepsilon}^T[\boldsymbol{J}_{h\varepsilon}^T\boldsymbol{M}_s\boldsymbol{J}_{h\varepsilon}\ddot{\boldsymbol{\varepsilon}} + \boldsymbol{J}_{h\varepsilon}^T\boldsymbol{M}_s\dot{\boldsymbol{J}}_{h\varepsilon}\dot{\boldsymbol{\varepsilon}} + \boldsymbol{C}_s\dot{\boldsymbol{\varepsilon}} + \boldsymbol{K}_s\boldsymbol{\varepsilon} - \boldsymbol{K}_s\boldsymbol{\varepsilon}_0 \\ &- (\boldsymbol{B}_{va} + \boldsymbol{B}_{vh})v] + \delta\boldsymbol{\varepsilon}^T(\boldsymbol{J}_{h\varepsilon}^T\boldsymbol{N}\boldsymbol{g} + \boldsymbol{J}_{p\varepsilon}^T\boldsymbol{B}^F\boldsymbol{F}^{\text{dist}} + \boldsymbol{J}_{\theta\varepsilon}^T\boldsymbol{B}^M\boldsymbol{M}^{\text{dist}} \\ &+ \boldsymbol{J}_{p\varepsilon}^T\boldsymbol{F}^{\text{pt}} + \boldsymbol{J}_{\theta\varepsilon}^T\boldsymbol{M}^{\text{pt}}) + \delta v(\boldsymbol{B}_{vh}^T\boldsymbol{\varepsilon} + C_p v + Q_e)\end{aligned} \tag{12}$$

Finally, the variations of the strain and the voltage are both arbitrary, which yields the electromechanical system's equations of motion,

$$\begin{aligned}&\boldsymbol{M}_{FF}\ddot{\boldsymbol{\varepsilon}} + \boldsymbol{C}_{FF}\dot{\boldsymbol{\varepsilon}} + \boldsymbol{K}_{FF}\boldsymbol{\varepsilon} = \boldsymbol{R}_F \\ &\boldsymbol{B}_{vh}^T\boldsymbol{\varepsilon} + C_p v + Q_e = 0 \quad \text{or} \quad \boldsymbol{B}_{vh}^T\dot{\boldsymbol{\varepsilon}} + C_p\dot{v} + \frac{v}{R_e} = 0\end{aligned} \tag{13}$$

where the generalized inertia, damping, stiffness matrices, and generalized force vector are

$$\begin{aligned}&\boldsymbol{M}_{FF}(\boldsymbol{\varepsilon}) = \boldsymbol{J}_{h\varepsilon}^T\boldsymbol{M}_s\boldsymbol{J}_{h\varepsilon} \quad \boldsymbol{C}_{FF}(\boldsymbol{\varepsilon},\dot{\boldsymbol{\varepsilon}}) = \boldsymbol{C} + \boldsymbol{J}_{h\varepsilon}^T\boldsymbol{M}_s\dot{\boldsymbol{J}}_{h\varepsilon} \quad \boldsymbol{K}_{FF} = \boldsymbol{K}_s \\ &\boldsymbol{R}_F = \boldsymbol{K}_{FF}\boldsymbol{\varepsilon}_0 + \boldsymbol{J}_{h\varepsilon}^T\boldsymbol{N}\boldsymbol{g} + \boldsymbol{J}_{p\varepsilon}^T\boldsymbol{B}^F\boldsymbol{F}^{\text{dist}} + \boldsymbol{J}_{\theta\varepsilon}^T\boldsymbol{B}^M\boldsymbol{M}^{\text{dist}} \\ &\quad + \boldsymbol{J}_{p\varepsilon}^T\boldsymbol{F}^{\text{pt}} + \boldsymbol{J}_{\theta\varepsilon}^T\boldsymbol{M}^{\text{pt}} + (\boldsymbol{B}_{va} + \boldsymbol{B}_{vh})v\end{aligned} \tag{14}$$

As shown in Eq. (14), the generalized force vector involves the effects from initial strains $\boldsymbol{\varepsilon}_0$, gravitational field $\boldsymbol{g}$, distributed forces $\boldsymbol{F}^{\text{dist}}$, distributed moments $\boldsymbol{M}^{\text{dist}}$, point forces $\boldsymbol{F}^{\text{pt}}$, point moments $\boldsymbol{M}^{\text{pt}}$, and the electric field v. The aerodynamic forces and moments are considered as distributed loads. Once the beam strain/curvature is solved from the equations of motion, the deformation of the beam reference line can be recovered from the kinematics [6,33].

D. Piezoelectric Actuation of Bending and Torsion Deformations

The multifunctional wing with embedded piezoelectric materials is also considered as a piezoelectric actuation device, in addition to the energy harvesting function discussed in the previous work [32]. Bent et al. [27] developed the anisotropic actuation equations using the conventional poling, which are followed in the current study.

With the in-plane structural anisotropy of the piezoelectric material and the assumption of plane stress ($T_3 = T_4 = T_5 = 0$), the piezoelectric constitutive relation in Eq. (1) becomes

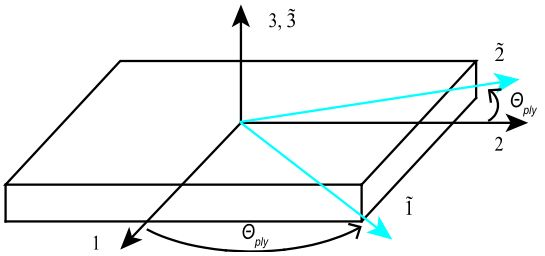

Fig. 4 Composite material axis and beam axis systems.

$$\begin{Bmatrix} \bar{\sigma}_1 \\ \bar{\sigma}_2 \\ \bar{\sigma}_6 \\ \bar{B}_3 \end{Bmatrix} = \begin{bmatrix} \bar{D}_{11} & \bar{D}_{12} & 0 & -e_{31} \\ \bar{D}_{12} & \bar{D}_{22} & 0 & -e_{32} \\ 0 & 0 & \bar{D}_{66} & 0 \\ e_{31} & e_{32} & 0 & \zeta_{33} \end{bmatrix} \begin{Bmatrix} \bar{\varepsilon}_1 \\ \bar{\varepsilon}_2 \\ \bar{\varepsilon}_6 \\ \bar{E}_3 \end{Bmatrix} \tag{15}$$

in which (1, 2, 3) are the beam axes and ($\tilde{1}$, $\tilde{2}$, $\tilde{3}$) are the piezoelectric material axes (see Fig. 4).

By applying the rotation of the material coordinate system from the beam coordinate system by a $+\theta$ angle about the 3-axis, the matrices in the constitutive relation become

$$\tilde{\bar{\boldsymbol{B}}} = \boldsymbol{T}_e \bar{\boldsymbol{B}} \quad \tilde{\boldsymbol{E}} = \boldsymbol{T}_e \boldsymbol{E} \quad \tilde{\bar{\boldsymbol{\varepsilon}}} = \boldsymbol{T}_s \bar{\boldsymbol{\varepsilon}} \quad \tilde{\bar{\boldsymbol{\sigma}}} = (\boldsymbol{T}_s^T)^{-1} \bar{\boldsymbol{\sigma}} \tag{16}$$

and

$$\begin{bmatrix} \bar{\boldsymbol{D}} & -\boldsymbol{e}^T \\ \boldsymbol{e} & \boldsymbol{\zeta} \end{bmatrix}_{\text{beam}} = \begin{bmatrix} \boldsymbol{T}_s^T \tilde{\boldsymbol{D}} \boldsymbol{T}_s & -\boldsymbol{T}_s^T \tilde{\boldsymbol{e}}^T \boldsymbol{T}_e \\ \boldsymbol{T}_e^T \tilde{\boldsymbol{e}} \boldsymbol{T}_s & \boldsymbol{T}_e^T \tilde{\boldsymbol{\zeta}} \boldsymbol{T}_e \end{bmatrix} \tag{17}$$

where the symbols with a tilde refer to the values in the piezoelectric material axes. $\boldsymbol{T}_s$ and $\boldsymbol{T}_e$ are the transformation matrices of composites [38].

For simplicity, the electric field and displacement are assumed to be along the 3-direction. The reduced constitutive relation in the beam system can be expressed as

$$\begin{Bmatrix} \bar{\boldsymbol{\sigma}} \\ \bar{B}_3 \end{Bmatrix} = \begin{bmatrix} \boldsymbol{T}_s^T \tilde{\boldsymbol{D}} \boldsymbol{T}_s & -\boldsymbol{T}_s \tilde{\boldsymbol{e}}^T \\ \tilde{\boldsymbol{e}} \boldsymbol{T}_s^T & \tilde{\zeta}_{33} \end{bmatrix} \begin{Bmatrix} \bar{\boldsymbol{\varepsilon}} \\ E_3 \end{Bmatrix} \tag{18}$$

According to Eq. (17), the piezoelectric coupling in the beam system is obtained as

$$\begin{aligned} \boldsymbol{e} &= \boldsymbol{T}_e^T \tilde{\boldsymbol{e}} \boldsymbol{T}_s \\ e_{31} &= \tilde{e}_{31}\cos^2\theta + \tilde{e}_{32}\sin^2\theta \\ e_{32} &= \tilde{e}_{31}\sin^2\theta + \tilde{e}_{32}\cos^2\theta \\ e_{36} &= \cos\theta \sin\theta(\tilde{e}_{31} - \tilde{e}_{32}) \end{aligned} \tag{19}$$

where e_{36} is the piezoelectric coupling for the induced shear stress. The piezoelectric induced stress can be obtained from Eq. (18) as

$$\bar{\boldsymbol{\sigma}}_{\text{pe}} = -\boldsymbol{T}_s^T \tilde{\boldsymbol{e}}^T E_3 \tag{20}$$

The resultant force and moment can be calculated from the piezoelectric induced terms. Bent et al. [27] developed the force and moment in thin-walled anisotropic composite structures using the Classical Laminated Plate Theory [38]. On the other hand, if the composite structure is a simple rectangular thin-walled section, one may choose an approach using the piezoelectric induced stresses to calculate the induced bending and torsional moments as in Ref. [28].

The coupling matrix $\boldsymbol{B}_{va}$ relates the actuation voltage and the resultant piezoelectric force and moment, given as

$$\begin{Bmatrix} B_{va1} \\ B_{va2} \\ B_{va3} \\ B_{va4} \end{Bmatrix} v = \begin{Bmatrix} F_{1a} \\ M_{1a} \\ M_{2a} \\ M_{3a} \end{Bmatrix} \tag{21}$$

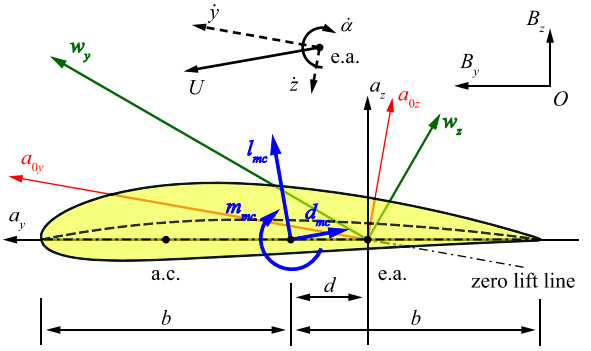

Fig. 5 Airfoil coordinate system and velocity components.

where F_{1a} is a piezoelectric induced extensional force, and M_{1a}, M_{2a}, and M_{3a} are piezoelectric induced moments about the 1, 2, and 3 axes, respectively. In this paper, the 1, 2, and 3 axes are oriented so that the coordinate is aligned with the wing beam coordinate axes x, y and z.

E. Unsteady Aerodynamics

The distributed loads $\boldsymbol{F}^{\text{dist}}$ and $\boldsymbol{M}^{\text{dist}}$ in Eq. (14) are divided into aerodynamic loads and user-supplied loads. The unsteady aerodynamic loads used in the current study are based on the two-dimensional (2D) finite-state inflow theory, provided by Peters and Johnson [37]. The theory calculates aerodynamic loads on a thin airfoil section undergoing large motions in an incompressible inviscid subsonic flow. The lift, moment, and drag of a thin 2D airfoil section about its midchord are given by

$$\begin{aligned} l_{\text{mc}} &= \pi\rho b^2(-\ddot{z} + \dot{y}\,\dot{\alpha} - d\ddot{\alpha}) + 2\pi\rho b\dot{y}^2\left[-\frac{\dot{z}}{\dot{y}} + \left(\frac{1}{2}b - d\right)\frac{\dot{\alpha}}{\dot{y}} - \frac{\lambda_0}{\dot{y}}\right] \\ m_{\text{mc}} &= 2\pi\rho b^2\left(-\frac{1}{2}\dot{y}\,\dot{z} - \frac{1}{2}d\dot{y}\,\dot{\alpha} - \frac{1}{2}\dot{y}\lambda_0 - \frac{1}{16}b^2\ddot{\alpha}\right) \\ d_{\text{mc}} &= -2\pi\rho b(\dot{z}^2 + d^2\dot{\alpha}^2 + \lambda_0^2 + 2d\dot{\alpha}\,\dot{z} + 2d\dot{\alpha}\lambda_0) \end{aligned} \tag{22}$$

where b is the semichord and d is the distance of the midchord in front of the reference axis. The quantity $-\dot{z}/\dot{y}$ is the angle of attack that consists of the contribution from both the steady-state angle of attack and the unsteady plunging motion of the airfoil. The different velocity components are shown in Fig. 5. The inflow velocity λ_0 accounts for induced flow due to free vorticity, which is the weighted summation of the inflow states λ as described by Peters and Johnson [37] and governed by

$$\dot{\boldsymbol{\lambda}} = \boldsymbol{F}_1\ddot{\boldsymbol{\varepsilon}} + \boldsymbol{F}_2\dot{\boldsymbol{\varepsilon}} + \boldsymbol{F}_3\boldsymbol{\lambda} \tag{23}$$

The aerodynamic loads about the midchord center are transferred to the wing elastic axis and rotated into the fixed B frame for the solution of equations of motion.

F. Feedback Control Algorithms

A LQR [34] (see Fig. 6) is commonly used in traditional aircraft control studies. To apply the linear control theory, the linearization of the nonlinear aeroelastic equations about a nonlinear equilibrium state is performed. The nonlinear aeroelastic equations of the cantilever wing are repeated here, without considering the gravity,

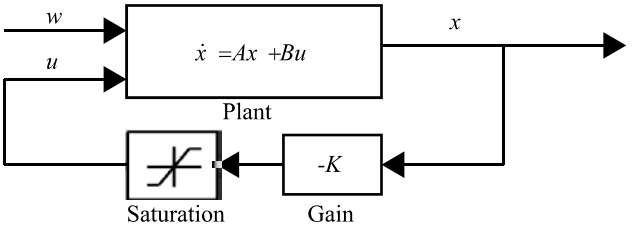

Fig. 6 LQR feedback control diagram.

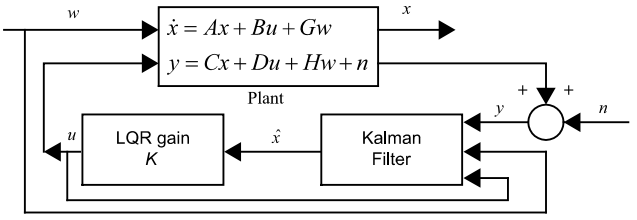

Fig. 7 LQG regulator feedback control diagram.

$$\boldsymbol{M}_{FF}\ddot{\boldsymbol{\varepsilon}} + \boldsymbol{C}_{FF}\dot{\boldsymbol{\varepsilon}} + \boldsymbol{K}_{FF}\boldsymbol{\varepsilon} = \boldsymbol{R}_F^{\text{aero}} + \boldsymbol{B}_v\boldsymbol{v} \quad \dot{\boldsymbol{\lambda}} = \boldsymbol{F}_1\ddot{\boldsymbol{\varepsilon}} + \boldsymbol{F}_2\dot{\boldsymbol{\varepsilon}} + \boldsymbol{F}_3\boldsymbol{\lambda} \tag{24}$$

and

$$\boldsymbol{R}_F^{\text{aero}} = \boldsymbol{J}_{p\varepsilon}^T\boldsymbol{B}_F\boldsymbol{F}^{\text{aero}} + \boldsymbol{J}_{\theta\varepsilon}^T\boldsymbol{B}_M\boldsymbol{M}^{\text{aero}} \tag{25}$$

where $\boldsymbol{R}_F^{\text{aero}}$ is the generalized aerodynamic load. $\boldsymbol{F}^{\text{aero}}$ and $\boldsymbol{M}^{\text{aero}}$ are the distributed aerodynamic lift and moment, respectively. $\boldsymbol{B}_v$ is the piezoelectric matrix, and $\boldsymbol{v}$ is electric voltage. The reference nonlinear equilibrium state where the linearization is performed is

$$\boldsymbol{x}_0 = \left\{\ddot{\boldsymbol{\varepsilon}}_0^T, \dot{\boldsymbol{\varepsilon}}_0^T, \boldsymbol{\varepsilon}_0^T, \boldsymbol{\lambda}_0^T\right\}^T \tag{26}$$

The structural Jacobians are assumed to be constant when the system is perturbed for the linearization, while this assumption holds for small perturbations to the system. This assumption helps to simplify the linearization process by making the generalized mass matrices independent of the state variables. Each equation is written with the small perturbation about the nonlinear equilibrium state, which yields

$$\begin{aligned}\bar{\boldsymbol{M}}_{FF}\ddot{\boldsymbol{\varepsilon}} + \bar{\boldsymbol{C}}_{FF}\dot{\boldsymbol{\varepsilon}} + \bar{\boldsymbol{K}}_{FF}\boldsymbol{\varepsilon} - \boldsymbol{R}_{F/\lambda_0}^{\text{aero}}\boldsymbol{\lambda} - \boldsymbol{B}_v\boldsymbol{v} &= \boldsymbol{0}\\ \dot{\boldsymbol{\lambda}} - \boldsymbol{F}_1\ddot{\boldsymbol{\varepsilon}} - \boldsymbol{F}_2\dot{\boldsymbol{\varepsilon}} - \boldsymbol{F}_3\boldsymbol{\lambda} &= \boldsymbol{0}\end{aligned} \tag{27}$$

where $\bar{\boldsymbol{M}}$, $\bar{\boldsymbol{C}}$, and $\bar{\boldsymbol{K}}$ are the linearized general inertia, damping, and stiffness matrices, respectively. $\boldsymbol{R}_{F/\lambda_0}^{\text{aero}}$ is the derivative of the aerodynamic load vector with respect to the inflow states. Equation (27) can be put into the state-space form

$$\dot{\boldsymbol{x}} = \boldsymbol{A}\boldsymbol{x} + \boldsymbol{B}\boldsymbol{u} \tag{28}$$

where

$$\boldsymbol{x} = \left\{\boldsymbol{\varepsilon}^T \quad \dot{\boldsymbol{\varepsilon}}^T \quad \boldsymbol{\lambda}^T\right\}^T \qquad \boldsymbol{u} = \boldsymbol{v} \tag{29}$$

where $\boldsymbol{v}$ is the input of piezoelectric actuation.

The associated quadratic performance index for control is defined as

$$J = \int_0^\infty \left(\boldsymbol{x}^T\boldsymbol{Q}\boldsymbol{x} + \boldsymbol{u}^T\boldsymbol{R}\boldsymbol{u}\right)\mathrm{d}t \tag{30}$$

where $\boldsymbol{R}$ and $\boldsymbol{Q}$ are positive-definite penalty matrices. The control gain $\boldsymbol{K}$ is determined by minimizing the cost function J in Eq. (30), and the control input $\boldsymbol{u}$ (or the piezoelectric actuation voltage $\boldsymbol{v}$) is determined by

$$\boldsymbol{u} = -\boldsymbol{K}\boldsymbol{x} \tag{31}$$

The LQR results in a robust closed-loop control system. However, the LQR design assumes all the states of the system are available for the feedback, which is not always true for most practical cases. The LQG regulator provides the compensation to the limitation of state variable availability. It also takes into account the process and measurement noises of the system. The LQG regulator consists of an LQR and a Kalman filter for the state estimation (see Fig. 7). The state-space model describing the problem is now given as

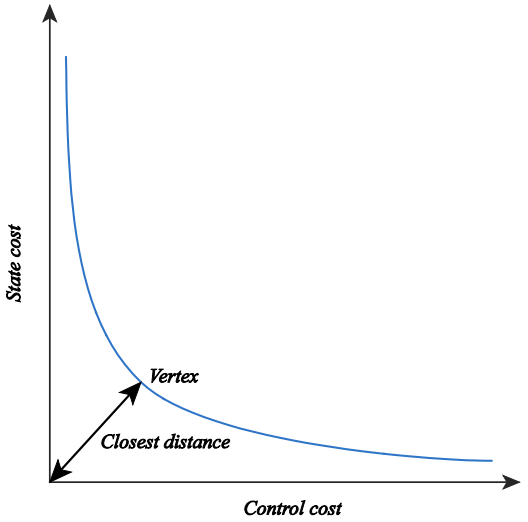

Fig. 8 State and control cost curve for finding the cost-effective point.

$$\dot{\boldsymbol{x}} = \boldsymbol{A}\boldsymbol{x} + \boldsymbol{B}\boldsymbol{u} + \boldsymbol{G}\boldsymbol{w} \quad \boldsymbol{y} = \boldsymbol{C}\boldsymbol{x} + \boldsymbol{D}\boldsymbol{u} + \boldsymbol{H}\boldsymbol{w} + \boldsymbol{n} \tag{32}$$

where $\boldsymbol{x}$ is the state vector, $\boldsymbol{u}$ is the control input to the system plant, $\boldsymbol{y}$ is a user-defined system output vector (wing spanwise bending and torsion curvatures in the current study), and $\boldsymbol{w}$ is the disturbance (process noise). Here, local strains are assumed to be measured by a certain sensor (e.g., strain gauges or piezoelectric sensors), with $\boldsymbol{n}$ being the possible sensor measurement noise. The noises $\boldsymbol{w}$ and $\boldsymbol{n}$ are zero-mean white noises. The Kalman filter provides an estimated $\hat{\boldsymbol{x}}$ to the state $\boldsymbol{x}$, such that the control input is obtained as

$$\boldsymbol{u} = -\boldsymbol{K}\hat{\boldsymbol{x}} \tag{33}$$

G. Weighted Control Penalty

The linear quadratic controllers minimize a certain performance index by applying penalties on both the states and control inputs. Different combinations of penalties may result in different control system performances. Therefore, it is important to establish an approach to evaluate the tradeoff and find a cost-effective controller setting.

Table 1 Wing properties

Airfoil	NACA0014
Span, cm	200
Chord length (at root), cm	20
Taper ratio	1:2
Reference axis location (from leading edge)	30% of chord
Center of gravity (from leading edge)	30% of chord

Table 2 Material properties for the wing layers

Property	E-Glass	AFC
E_1, GPa	19.3	42.2
E_2, GPa	19.3	17.5
E_3, GPa	9.8	17.5
G_{12}, GPa	4.1	5.5
G_{13}, GPa	4.1	5.5
G_{23}, GPa	3.28	4.4
v_{12}	0.148	0.354
v_{13}	0.148	0.354
v_{23}	0.207	0.496
Thickness, mm	0.1143	0.127
d_{11}, pm/V	— —	309
d_{12}, pm/V	— —	−129
Electrode distance, mm	— —	1.143

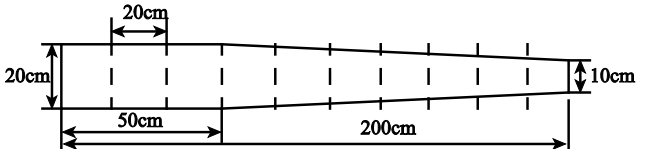

Fig. 9 Wing dimensions.

A good approach to evaluate the performance is to normalize the cost function and to split them into two components of state variables and control inputs, respectively, which can be defined as the state cost J_s and the control cost J_c [39]. The objective cost function defined in Eq. (30) can be rewritten with an additional weighting term r:

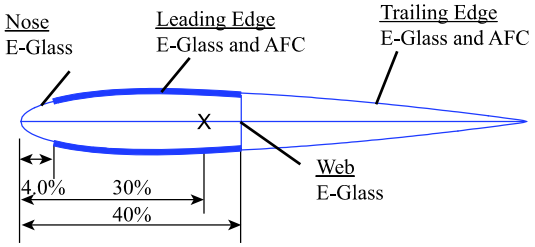

Fig. 10 Layups of the wing cross-section (AFC, active fiber composite).

$$J = \int_0^\infty (\boldsymbol{x}^T \boldsymbol{Q}\boldsymbol{x} + r\boldsymbol{u}^T \boldsymbol{R}\boldsymbol{u})\mathrm{d}t \tag{34}$$

This cost function has two contributors as

$$J_s = \int_0^\infty (\boldsymbol{x}^T \boldsymbol{Q}\boldsymbol{x})\mathrm{d}t \quad J_c = \int_0^\infty (\boldsymbol{u}^T \boldsymbol{R}\boldsymbol{u})\mathrm{d}t \tag{35}$$

To have the kinetic and strain energy form of the system in the state cost, $\boldsymbol{Q}$ can be defined as

$$\boldsymbol{Q} = \begin{bmatrix} \boldsymbol{K}_s & \boldsymbol{0} \\ \boldsymbol{0} & \boldsymbol{M}_s \end{bmatrix} \tag{36}$$

The control cost is the integral of actuation energy with respect to time. In the design process, J_s and J_c are obtained by solving Lyapunov and Riccati equations [39]. The weighting r in Eq. (34) is to control the penalty balance between state cost and control cost. Using this weighting value, the state and control costs can be normalized as

$$J_S = J_s \quad J_C = \frac{J_c}{r} \tag{37}$$

As a preliminary design, the approach used in Ref. [39] is applied here to determine a balanced control setting between the state and control costs. Figure 8 exemplifies the normalized cost functions to determine a feasible preliminary design point. The balanced penalty

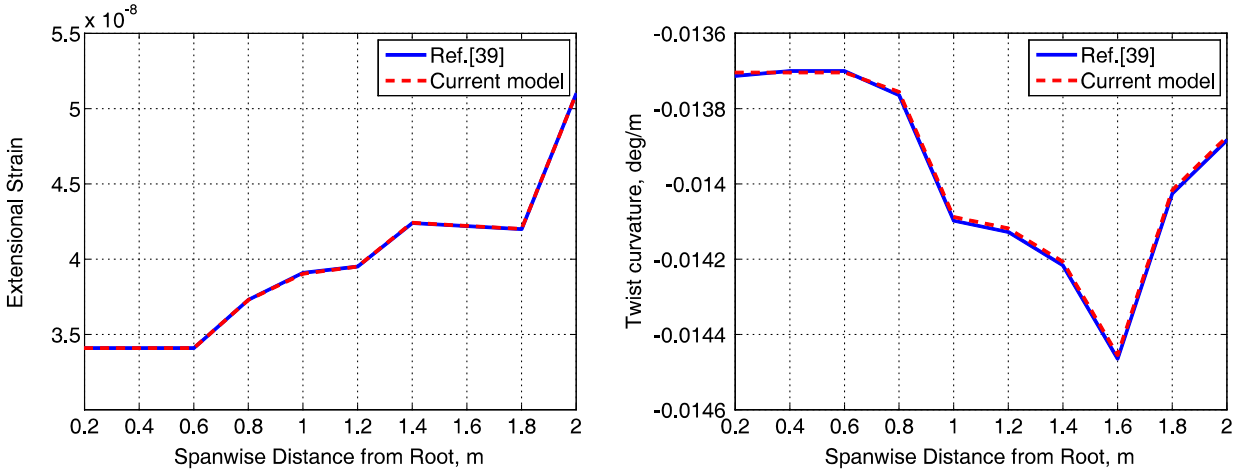

Fig. 11 Extensional strain and twist curvature of the active wing with static voltage actuation.

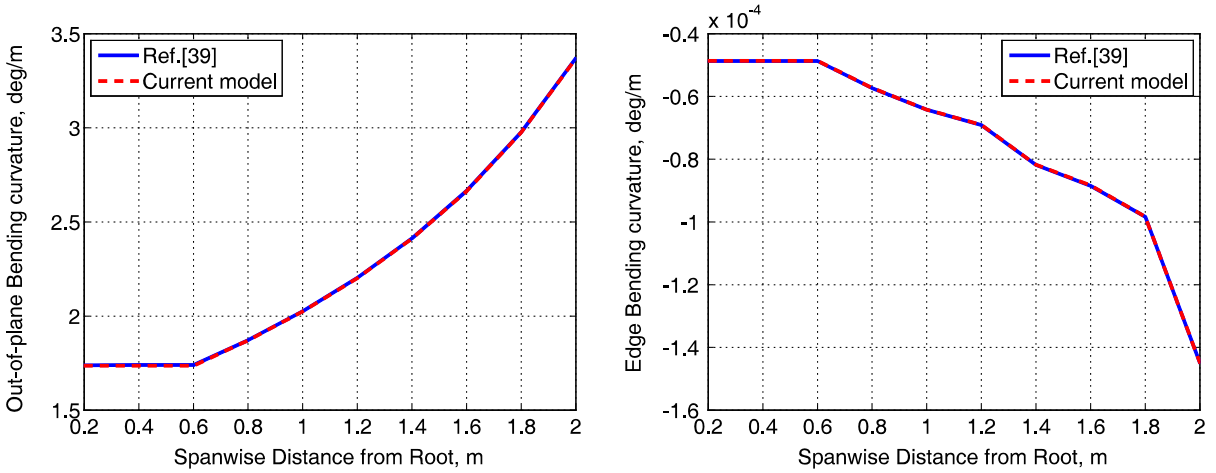

Fig. 12 Out-of-plane and edge bending curvatures of the active wing with static voltage actuation.

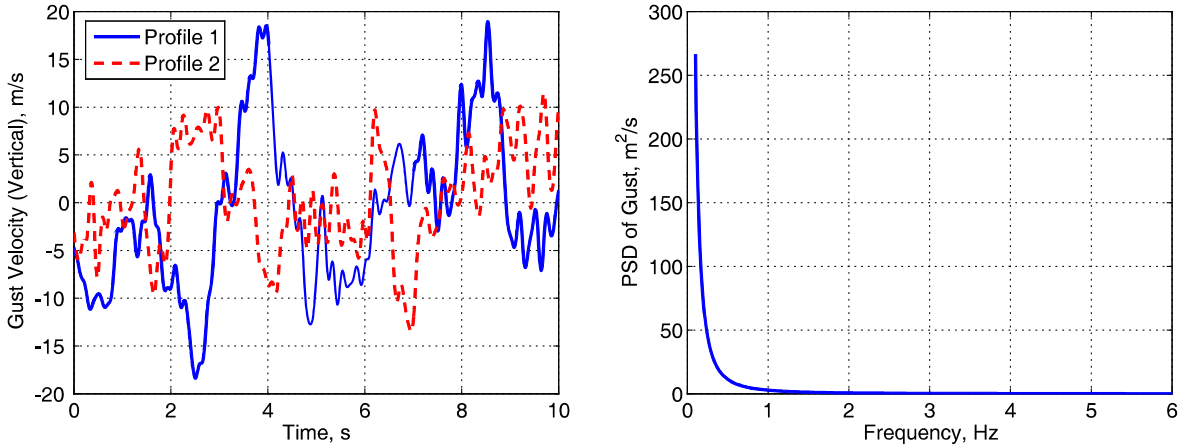

Fig. 13 Gust velocity profiles and PSD function.

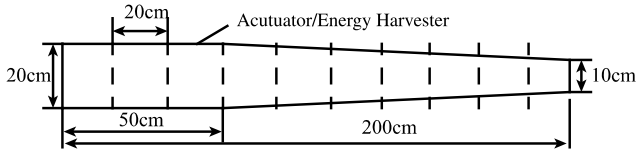

Fig. 14 Partition of the multifunctional wing.

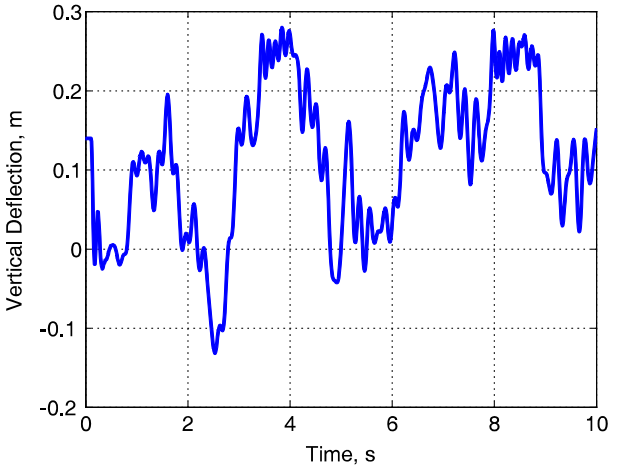

Fig. 15 Wing tip deflection with gust profile 1.

point, or cost effective point, can be found at the vertex of the hyperbolic curve.

III. Numerical Verification of Anisotropic Piezoelectric Actuation

In this section, the anisotropic actuation model implemented in the strain-based beam formulation is validated, while other aspects of the complete formulation, such as the aeroelastic formation [4,5] and piezoelectric energy harvesting [32], have been validated or verified in previous studies. For this purpose, the composite wing studied in Ref. [39] is modeled here. While the detailed wing properties can be found in Ref. [39], Tables 1 and 2 list the basic geometric and material properties of the wing. Figure 9 shows the wing geometry, and Fig. 10 highlights the layups of the wing cross-section. A single passive wing spar is built at 40% chord from the leading edge within the wing cross-section.

Although the studies in Ref. [39] covered different actuator orientations from 0 to ±45 deg, only the actuation oriented at ±22 deg is performed in the current study to have the balanced bending and torsional actuation capability.

Figures 11 and 12 compare the extensional strain, twist, out-of-plane, and edge bending curvatures from the current simulation and those from Ref. [39] with a 2000 V static actuation voltage. After a convergence study, the wing is divided into ten strain-based beam elements in the current simulation, with three elements in the uniform segment and seven in the tapered segment. Gravity and aerodynamic loads are not included as Ref. [39]. Overall, there is an excellent agreement between the two sets of results.

IV. Numerical Studies

Nonlinear active aeroelastic analysis results are presented here for the slender wing studied in the previous section, which are obtained by using the derived electroaeroelastic formulation. Feedback controls of wing vibrations due to gust disturbances are also discussed. Particularly, concurrent active piezoelectric actuation and energy harvesting are explored with the wing model. In doing so, a parametric study of the impact of the piezoelectric actuator and energy harvester placement on the wing performance will be presented, where both the effectiveness of gust alleviation and the voltage output from the multifunctional wing will be simultaneously explored.

Table 4 List of different multifunctional wing configurations

	Configuration			
Function	1	2	3	4
Actuator element ID	1–10	1–5	1–3	1
Harvester element ID	— —	6–10	7–10	2–10

Table 3 RMS bending and twist curvatures on each wing element with gust perturbation

	Element									
State variable	1	2	3	4	5	6	7	8	9	10
Flat bending curvature (m^{-1})	0.1250	0.0977	0.0742	0.0668	0.0583	0.0486	0.0376	0.0253	0.0127	0.0028
Twist curvature ($\times 10^{-4}$ m^{-1})	20.105	14.653	10.920	10.008	9.2634	8.5939	7.8640	6.8714	5.2754	2.3794

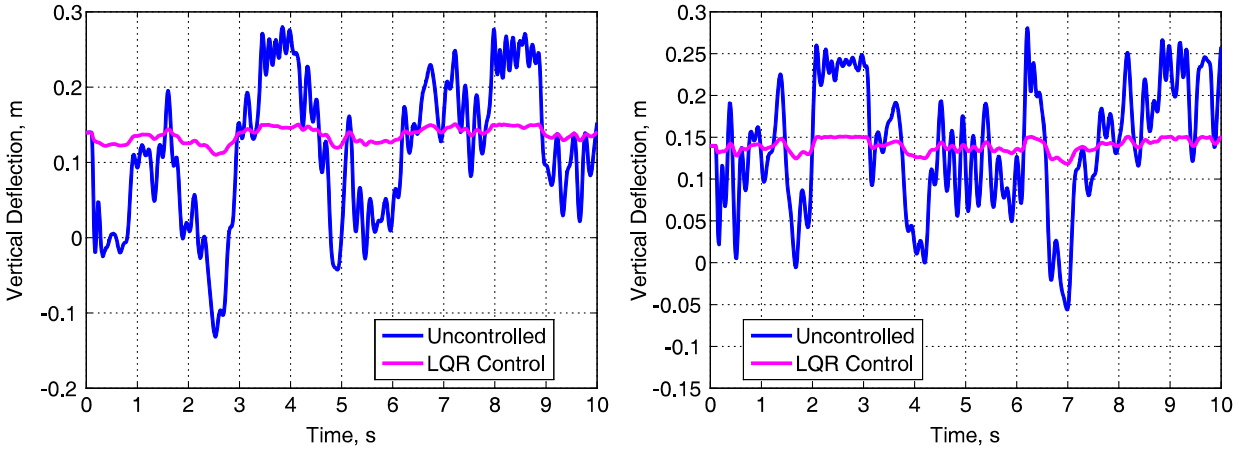

Fig. 16 Wing tip deflections with LQR controller under gust profiles 1 (left) and 2 (right) for wing configuration 1.

A. Gust Model and Wing Actuator and Energy Harvester Design

To evaluate the wing behavior under stochastic gust perturbations, two different gust signals are generated based on the power spectral density (PSD) function of the Dryden gust model with the gust strength of 30 m/s, the velocity profiles of which are plotted in Fig. 13. The freestream velocity is 70 m/s, and the altitude is 15,000 m. This flight condition is used in all the following studies. Note a detailed description of implementing the Dryden gust model was provided in Ref. [32].

The wing model studied in the previous section is used here to design the multifunctional wing. The wing is still divided into ten elements, all with the embedded piezoelectric material. They can all be flexibly designated as either active actuators for the vibration control or harvesters for the energy conversion. Figure 14 describes the conceptual multifunctional wing design. To determine the effective actuator and energy harvester placement, the wing vibration with the gust perturbation is first simulated with no piezoelectric effects. A time step of 0.01 s is used in all time-domain simulations with a cantilever boundary condition. Figure 15 shows the uncontrolled wing tip vertical deflection over 10 s with gust profile 1 (see Fig. 13) and an 8 deg angle of attack. Table 3 lists the rms bending and twist curvatures of each wing element during the 10 s simulation. According to the wing deformation, the wing portion closer to the root exhibits larger bending and twist curvatures, compared to the tip portion. Therefore, it is more efficient to put the controllers closer to the wing root for a better vibration control. The rest of the wing elements can then be used as energy harvesters. Alternatively, one may want to use an opposite configuration to maximize the output voltage from energy harvesters if the wing vibration is allowed and more energy output is desired. In this paper, the priority is given to the wing vibration control. For parametric study purposes, four different wing configurations are considered in the current study listed in Table 4, where element identifiers (IDs) are assigned from the wing root to the tip, ranging from 1 to 10. Lastly, the piezoelectric resistance load of the energy harvesting circuit is set to be 1 MΩ.

B. Gust Suppression Using LQR

The wing active control study starts by using the wing configuration with full-span actuators (configuration 1). To evaluate the controllers' effectiveness with different gust perturbations, both gust profiles 1 and 2 are applied. The wing tip vertical deflections with the designed LQR controller under gust profiles 1 and 2, respectively, are shown in Fig. 16. As is done in traditional gust control studies, one may design a controller to suppress the gust vibration as much as possible. In this case, the weighting parameter r for the LQR controller is 5.00×10^{-10}, resulting in an effective gust suppression. Table 5 gives the list of the original state and control costs of the simulations [calculated by using Eq. (35)]. The state cost reduction with respect to the uncontrolled vibration is used to measure the performance of the vibration control since it is essentially a summation of the wing vibrational kinetic energy and strain energy. One can find a 98.90% and a 98.96% state cost reduction, respectively, by applying the LQR controller under the two gusts. However, this suppression is achieved at the cost of a significant amount of control effort. This can be observed from Table 6, which lists the rms voltage inputs for each actuator during the simulation.

C. Integral Multifunctional Wing for Concurrent Active Control and Energy Harvesting

As discussed before, for concurrent active actuation and energy harvesting of the multifunctional wing, one does not need to push to the limit to minimize the wing vibration. If a certain magnitude of wing vibration is allowed and it does not significantly impact wing

Table 5 State and control costs on wing configuration 1 under both gust profiles

Gust profile	Cost, J · s	No control	LQR controller	State cost reduction, %
1	State cost	29.78	0.33	98.90
	Control cost, $\times 10^8$	— —	5.96	— —
2	State cost	17.04	0.18	98.96
	Control cost, $\times 10^8$	— —	3.22	— —

Table 6 RMS voltage input (V_{rms}, V) along wing configuration 1

	Element ID									
Gust profile	1	2	3	4	5	6	7	8	9	10
1	4913.1	3810.1	2868.6	2373.0	1894.6	1433.1	994.1	593.3	261.2	50.4
2	3603.5	2796.9	2108.4	1746.7	1396.9	1058.5	735.6	440.0	194.1	37.6

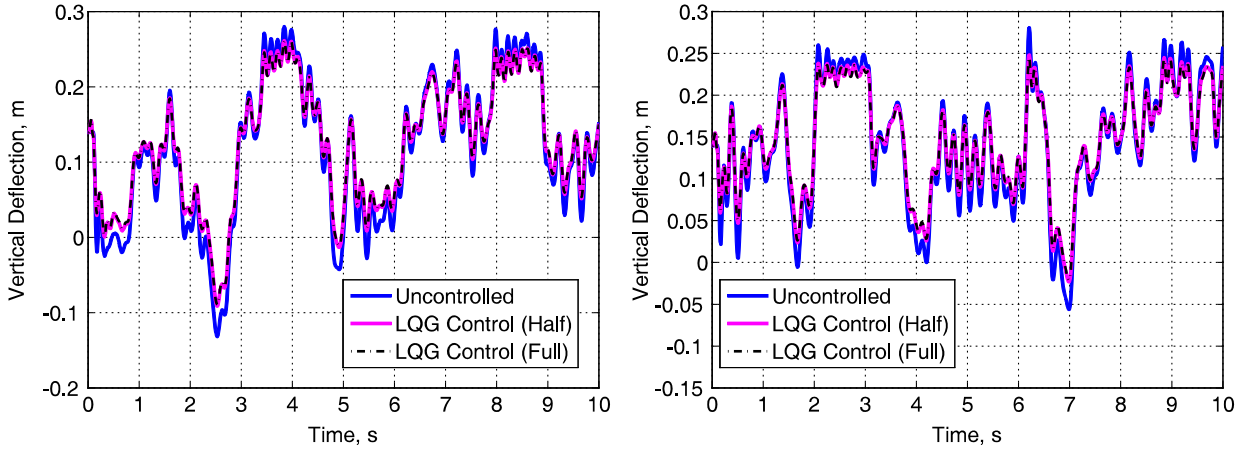

Fig. 17 Wing tip deflections with the LQG controller with gust profiles 1 (left) and 2 (right).

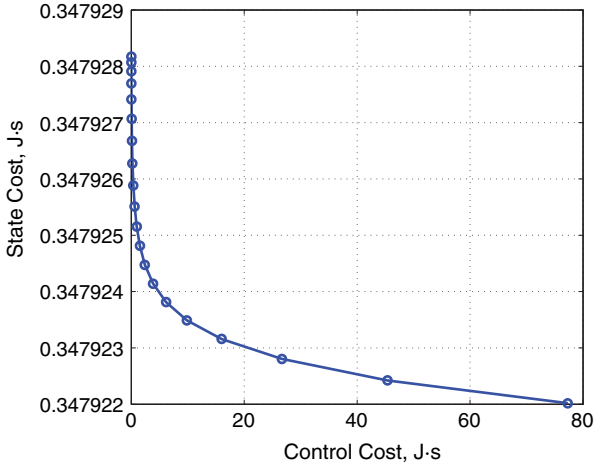

Fig. 18 State and control costs for LQG controller design.

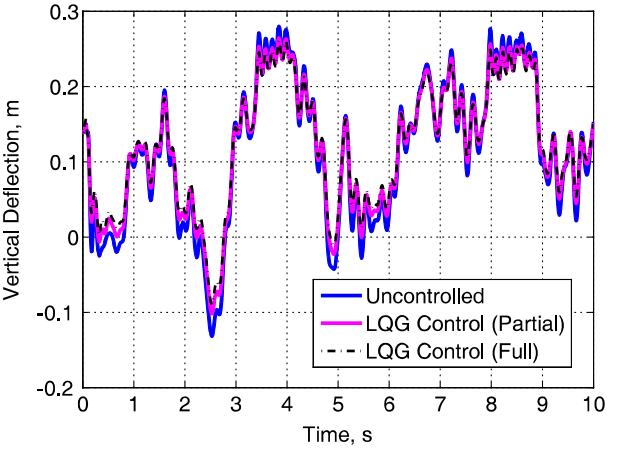

Fig. 19 Wing tip deflections with gust profile 1 for wing configuration 3.

and aircraft flight performance, this vibration could be converted to the electric energy by using the piezoelectric effects. For this purpose, the second wing configuration with the half-span actuators (configuration 2 in Table 4) and harvesters is also considered. With both gust profiles applied to both wing configurations 1 and 2, the wing behaviors are simulated and shown in Fig. 17. Only the LQG controller is studied in this and the following cases, as it is more practical use real applications. As the aim of this study is to explore

Table 7 RMS voltage input/output (V_{rms}, V) of wing configurations 1 and 2

Wing configuration	Gust profile	V_{rms}	Element ID 1	2	3	4	5	6	7	8	9	10	Total
1	1	Harvest output, V	— —	— —	— —	— —	— —	— —	— —	— —	— —	— —	— —
		Actuation input, V	1068.5	818.35	581.93	440.76	333.08	249.16	178.64	113.80	53.90	10.81	3848.9
	2	Harvest output, V	— —	— —	— —	— —	— —	— —	— —	— —	— —	— —	— —
		Actuation input, V	822.65	615.10	442.30	341.76	262.44	197.77	141.50	89.49	42.14	8.46	2963.6
2	1	Harvest output, V	— —	— —	— —	— —	— —	3.16	2.05	1.13	0.46	0.08	6.89
		Actuation input, V	973.64	778.95	610.13	534.06	469.78	— —	— —	— —	— —	— —	3366.6
	2	Harvest output, V	— —	— —	— —	— —	— —	2.44	1.58	0.88	0.36	0.06	5.32
		Actuation input	746.55	587.37	462.79	405.65	357.07	— —	— —	— —	— —	— —	2559.4

Table 8 State and control costs of wing configurations 1 and 2 under two gust profiles

Wing configuration	Gust profile	Cost, J · s	No control	LQG controller	State cost reduction, %
1	1	State cost	29.78	19.98	32.91
		Control cost, $\times 10^7$	— —	2.57	— —
	2	State cost	17.04	11.36	33.32
		Control cost, $\times 10^7$	— —	1.51	— —
2	1	State cost	29.78	20.43	31.39
		Control cost, $\times 10^7$	— —	2.44	— —
	2	State cost	17.04	11.66	31.56
		Control cost, $\times 10^7$	— —	1.41	— —

Table 9 RMS voltage input/output (V_{rms}, V) with wing configuration 3

	Element ID										
Actuation input V_{rms}, V	1	2	3	4	5	6	7	8	9	10	Total
Harvest output	— —	— —	— —	5.89	4.45	3.16	2.05	1.14	0.46	0.08	17.24
Actuation input	846.61	755.94	699.63	— —	— —	— —	— —	— —	— —	— —	2301.9

Table 10 State and control costs of wing configuration 3 under gust profile 1

Cost, J · s	No control	LQG controller	State cost reduction, %
State cost	29.78	22.39	24.83
Control cost, $\times 10^7$	— —	1.78	— —

the dual functions of the multifunctional wing, the controllers are designed to have a balanced control performance with the weight parameter r being 8.86×10^{-8} (around the vertex of the cost curve in Fig. 18). Table 7 lists the rms voltage inputs/outputs on each element, while the simple summation of the rms voltage outputs is called the total output. Note a more accurate estimation of the total voltage output depends on the system's circuit, which is not discussed herein. Over the 10 s simulation, wing configuration 2 accumulates a total voltage output of 6.89 and 5.32 V with the two applied profiles, respectively. Additionally, the required actuation voltage input also drops from configuration 1 to configuration 2. Therefore, using the second wing configuration saves energy. One can further evaluate the vibration reduction performance of the two configurations by comparing the states and control costs, which are listed in Table 8. Obviously, the state cost reductions of the two configurations are very close. Therefore, wing configuration 2 with the corresponding LQG controller has almost the same vibration control performance, at a lower voltage input with some additional energy savings. This configuration takes advantage of the dual functions of the multifunctional wing.

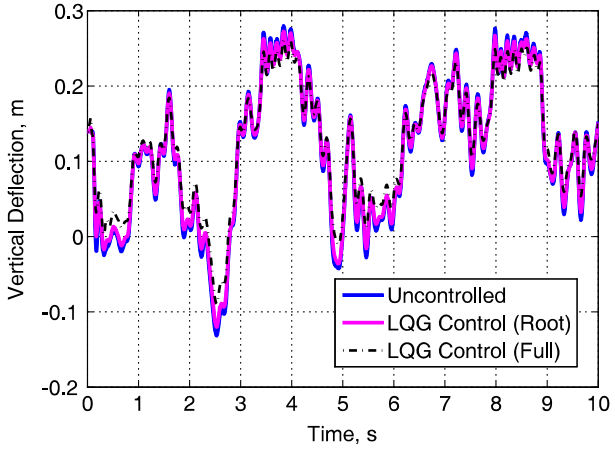

Fig. 20 Wing tip deflections with gust profile 1 for wing configuration 4.

In the next study, the number of wing actuators is further reduced to 3 (see Table 4 for wing configuration 3), while the energy harvesters occupy from 30% to the full span of the wing. Since the two gust profiles do not introduce qualitatively different wing behaviors, only gust profile 1 is used from now on. The wing tip deflection with the gust perturbation is plotted in Fig. 19, which is also compared with those of the uncontrolled wing and the one with full-span actuators. It can be seen that, even if the number of actuators is reduced from 10 to 3, the controller still maintains the gust alleviation capability. The output/input voltage from each harvester/actuator and the total voltage over the 10 s are listed in Table 9. The total output voltage from the harvesters is 17.24 V, which might be available for some low-power sensors' operation. However, the required control actuation voltage is still much higher than the harvester output. Thus, an additional power supply would be required for the actuation. The state and control costs with the LQG controller are listed in Table 10. The state cost reduction of the wing with partial-span actuators is 24.83%.

Finally, wing configuration 4 is applied in the study, where only the root element is an actuator and the rest of the elements are used as harvesters. Figure 20 shows the controlled wing tip deflections of wing configurations 1 and 4 with gust profile 1. They are also compared to the uncontrolled wing response. The corresponding voltage outputs from the energy harvesters and the required actuation

Table 11 RMS voltage output/input (V_{rms}, V) with wing configuration 4

	Element ID (from root)										
Actuation input V_{rms}, V	1	2	3	4	5	6	7	8	9	10	Total
Harvest output	— —	9.84	7.48	5.91	4.47	3.18	2.06	1.14	0.46	0.08	34.61
Actuation input	795.50	— —	— —	— —	— —	— —	— —	— —	— —	— —	795.50

Table 12 State and control costs of wing configuration 4 under gust profile 1

Cost, J · s	No control	LQG controller	State cost reduction, %
State cost	29.78	26.56	10.82
Control cost, $\times 10^6$	— —	6.33	— —

Table 13 Comparison of the multifunctional wing performance

Wing configuration	Output voltage, V	Input voltage, V	Control cost, J · s × 10^7	State cost, J · s	State cost reduction, %
1	— —	3848.9	2.57	19.98	32.91
2	6.89	3366.6	2.44	20.43	31.39
3	17.24	2301.9	1.78	22.39	24.83
4	34.61	795.50	0.63	26.56	10.82

voltage inputs for the gust control are listed in Table 11. As can be seen from the results, the control effectiveness is further reduced with the reduction of the actuated elements, while the harvested energy is more than doubled, and the required total actuation voltage is reduced to less than half to the wing configuration 3. The state and control costs of wing configuration 4 are given in Table 12. The state cost reduction of wing configuration 4 is 10.82%.

A final summary of the performance of the different multifunctional wing configurations with gust profile 1 using the LQG controller is provided in Table 13, where the energy harvesting output, vibration control voltage input, control cost, and state cost are all compared. From the table, one can clearly see the variation trend of the performance of the different wing configurations. The wing is migrating from a control dominant configuration to a configuration with more energy output.

V. Conclusions

An approach for the integral modeling of energy harvesting from wing transient vibrations and bending/torsional actuation with anisotropic piezoelectric materials was introduced in the paper. The strain-based geometrically nonlinear beam formulation, which makes no approximation to the deformation of the beam reference line, was coupled with an electromechanical model of the piezoelectric effect. For aeroelastic analysis, the finite-state unsteady aerodynamic model developed by Peters et al. [37] is used to calculate the aerodynamic loads on the wing surface. The coupled electroaeroelastic model enables the prediction of the transient electric outputs and the mechanical deformations of the electro-aeroelastic system under external excitations. The nonlinear electroaeroelastic formulation is suitable for both the active piezoelectric actuation and energy harvesting studies for highly flexible wings. Based on the formulation, linear quadratic regulator (LQR) and linear quadratic Gaussian (LQG) regulator controllers were implemented to regulate the piezoelectric actuation.

The actuation model was validated by comparing it with the published results. Excellent agreement was obtained. A LQR controller was initially designed for the gust alleviation of a multifunctional wing. It demonstrated an effective suppression of the wing vibration due to the gust perturbation. However, this wing configuration did not take full advantage of the multifunctional wing. Therefore, in the following studies, concurrent actuation for gust control and energy harvesting were studied using piezoelectric transducers. Because of the difficulty in obtaining all the system states in real applications, the LQG regulator controller was also studied, where the Kalman filter provided the state estimation of the system. Furthermore, the LQG regulator penalty was determined to have a balanced, cost-effective control. In the study, the actuator and energy harvester placement of the multifunctional wing was designed based on the dominant deformation due to the gust disturbance, with the priority given to the effectiveness of the gust alleviation over the energy harvesting output. The dual-functional wing still maintained its gust alleviation capability, while providing output from the energy harvesters with the reduced control actuators. With the stronger gust disturbances, the system was expected to provide enough voltage to support a low-power sensor operation.

From the study, one can see the piezoelectric multifunctional wing can be properly designed to maintain the wing vibration control capability while providing a certain level of electric energy output. This requires an optimal design of the placement (or actuation scheme) of the piezoelectric actuator and energy harvester, which was not performed in the current study. The penalties of the LQG controller were determined based on a balance between the state and control costs, which were not fully optimized, either. That caused the gust suppression performance of the studied multifunctional wings to drop far below the first study with the LQR controller. Therefore, on top of the individual subsystems of the multifunctional wing, an optimal control algorithm needs to be designed to integrate all the subsystems, targeting the effectiveness of the vibration control with the minimum energy consumption and maximum energy output.

References

[1] Tilmann, C. P., Flick, P. M., Martin, C. A., and Love, M. H., "High-Altitude Long Endurance Technologies for SensorCraft," *Symposium on Novel and Emerging Vehicle and Vehicle Technology Concepts, RTO-AVT-099*, NATO's Research and Technology Organisation (RTO) MP-104-P-26, Brussels, April 2003.

[2] Patil, M. J., Hodges, D. H., and Cesnik, C. E. S., "Nonlinear Aeroelasticity and Flight Dynamics of High-Altitude Long-Endurance Aircraft," *Journal of Aircraft*, Vol. 38, No. 1, 2001, pp. 88–94. doi:10.2514/2.2738

[3] Shearer, C. M., and Cesnik, C. E. S., "Nonlinear Flight Dynamics of Very Flexible Aircraft," *Journal of Aircraft*, Vol. 44, No. 5, 2007, pp. 1528–1545. doi:10.2514/1.27606

[4] Su, W., and Cesnik, C. E. S., "Nonlinear Aeroelasticity of a Very Flexible Blended-Wing-Body Aircraft," *Journal of Aircraft*, Vol. 47, No. 5, 2010, pp. 1539–1553. doi:10.2514/1.47317

[5] Su, W., and Cesnik, C. E. S., "Dynamic Response of Highly Flexible Flying Wings," *AIAA Journal*, Vol. 49, No. 2, 2011, pp. 324–339. doi:10.2514/1.J050496

[6] Cesnik, C. E. S., and Brown, E. L., "Modeling of High Aspect Ratio Active Flexible Wings for Roll Control," *43rd AIAA/ASME/ASCE/AHS Structures, Structural Dynamics, and Materials Conferences*, AIAA Paper 2002-1719, 2002.

[7] Cesnik, C. E. S., and Su, W., "Nonlinear Aeroelastic Modeling and Analysis of Fully Flexible Aircraft," *46th AIAA/ASME/ASCE/AHS/ASC Structures, Structural Dynamics, and Materials Conference*, AIAA Paper 2005-2169, April 2005.

[8] Chang, C.-S., Hodges, D. H., and Patil, M. J., "Flight Dynamics of Highly Flexible Aircraft," *Journal of Aircraft*, Vol. 45, No. 2, 2008, pp. 538–545. doi:10.2514/1.30890

[9] Pendleton, E., Flick, P., Paul, D., Voracek, D. F., Reichenbach, E., and Griffin, K., "The X-53 A Summary of the Active Aeroelastic Wing Flight Research Program," *48th AIAA/ASME/ASCE/AHS/ASC Structures, Structural Dynamics and Materials Conference and Exhibit*, AIAA Paper 2007-1855, April 2007.

[10] Voracek, D. F., Pendleton, E., Reichenbach, E., Griffin, K., and Welch, L., "The Active Aeroelastic Wing Phase I Flight Research Through January 2003," NASA TM-2003-210741, 2004.

[11] Christodoulou, L., and Venables, J. D., "Multifunctional Material Systems: The First Generation," *Journal of the Minerals Metals and Materials Society*, Vol. 55, No. 12, 2003, pp. 39–45. doi:10.1007/s11837-003-0008-z

[12] Anton, S. R., Erturk, A., and Inman, D. J., "Multifunctional Unmanned Aerial Vehicle Wing Spar for Low-Power Generation and Storage," *Journal of Aircraft*, Vol. 49, No. 1, 2012, pp. 292–301. doi:10.2514/1.C031542

[13] Bent, A. A., "Active Fiber Composite Material Systems for Structural Control Applications," *Smart Structures and Materials 1999: Industrial and Commercial Applications of Smart Structures Technologies*, Vol. 3674, SPIE, Bellingham, WA, 1999, pp. 166–177.

[14] Williams, R. B., Park, G., Inman, D. J., and Wilkie, W. K., "An Overview of Composite Actuators with Piezoceramic Fibers," *20th International Modal Analysis Conference*, Vol. 4753, Soc. for Experimental Mechanics (SEM), Bethel, CT, Feb. 2002, pp. 421–427.

[15] Erturk, A., and Inman, D. J., *Piezoelectric Energy Harvesting*, Wiley, Hoboken, NJ, 2011, pp. 1–94,151–385.

[16] Karami, M. A., and Inman, D. J., "Equivalent Damping and Frequency Change for Linear and Nonlinear Hybrid Vibrational Energy Harvesting Systems," *Journal of Sound and Vibration*, Vol. 330, No. 23, 2011, pp. 5583–5597. doi:10.1016/j.jsv.2011.06.021

[17] Tan, Y. K., and Panda, S. K., "Energy Harvesting from Hybrid Indoor Ambient Light and Thermal Energy Sources for Enhanced Performance of Wireless Sensor Nodes," *IEEE Transactions on Industrial Electronics*, Vol. 58, No. 9, 2011, pp. 4424–4435. doi:10.1109/TIE.2010.2102321

[18] De Marqui, C., Vieira, W. G. R., Erturk, A., and Inman, D. J., "Modeling and Analysis of Piezoelectric Energy Harvesting from Aeroelastic Vibrations Using the Doublet-Lattice Method," *Journal of Vibration and Acoustics*, Vol. 133, No. 1, 2011, pp. 9–25. doi:10.1115/1.4002785

[19] Roundy, S., and Wright, P. K., "A Piezoelectric Vibration Based Generator for Wireless Electronics," *Smart Materials and Structures*, Vol. 13, No. 5, 2004, pp. 1131–1142. doi:10.1088/0964-1726/13/5/018

[20] Dutoit, N. E., Wardle, B. L., and Kim, S. G., "Design Considerations for MEMS-Scale Piezoelectric Mechanical Vibration Energy Harvesters,"

Integrated Ferroelectrics, Vol. 71, No. 1, 2005, pp. 121–160. doi:10.1080/10584580590964574

[21] Bilgen, O., Wang, Y., and Inman, D. J., "Electromechanical Comparison of Cantilevered Beams with Multifunctional Piezoceramic Devices," *Mechanical Systems and Signal Processing*, Vol. 27, No. 1, 2012, pp. 763–777. doi:10.1016/j.ymssp.2011.09.002

[22] Wang, Y., and Inman, D. J., "Simultaneous Energy Harvesting and Gust Alleviation for a Multifunctional Composite Wing Spar Using Reduced Energy Control via Piezoceramics," *Journal of Composite Materials*, Vol. 47, No. 1, 2013, pp. 125–146. doi:10.1177/0021998312448677

[23] Sodano, H. A., Park, G., and Inman, D. J., "Estimation of Electric Charge Output for Piezoelectric Energy Harvesting," *Strain*, Vol. 40, No. 2, 2004, pp. 49–58. doi:10.1111/str.2004.40.issue-2

[24] Hagood, N. W., Chung, W. H., and von Flotow, A., "Modelling of Piezoelectric Actuator Dynamics for Active Structural Control," *Journal of Intelligent Material Systems and Structures*, Vol. 1, No. 3, 1990, pp. 327–354. doi:10.1177/1045389X9000100305

[25] Crawley, E. F., and Anderson, E. H., "Detailed Models of Piezoceramic Actuation of Beams," *Journal of Intelligent Material Systems and Structures*, Vol. 1, No. 1, 1990, pp. 4–25. doi:10.1177/1045389X9000100102

[26] Erturk, A., and Inman, D. J., "Issues in Mathematical Modeling of Piezoelectric Energy Harvesters," *Smart Materials and Structures*, Vol. 17, No. 6, 2008, pp. 1–14. doi:10.1088/0964-1726/17/6/065016

[27] Bent, A. A., Hagood, N. W., and Rodgers, J. P., "Anisotropic Actuation with Piezoelectric Fiber Composites," *Journal of Intelligent Material Systems and Structures*, Vol. 6, No. 3, 1995, pp. 338–349. doi:10.1177/1045389X9500600305

[28] Wilkie, W. K., Belvin, W. K., and Park, K. C., "Aeroelastic Analysis of Helicopter Rotor Blades Incorporating anisotropic Piezoelectric Twist Actuation," *ASME 1996 World Congress and Exposition*, Vol. 52, American Soc. of Mechanical Engineers, New York, 1996, pp. 423–434.

[29] Cesnik, C. E. S., and Ortega-Morales, M., "Active Beam Cross-Sectional Modeling," *Journal of Intelligent Material Systems and Structures*, Vol. 12, No. 7, 2001, pp. 483–496. doi:10.1177/10453890122145285

[30] Cesnik, C. E. S., and Shin, S., "Structural Analysis for Designing Rotor Blades with Integral Actuators," *39th Structures, Structural Dynamics, and Materials Conference*, AIAA Paper 1998-2107, April 1998.

[31] Du Plessis, A. J., "Modeling and Experimental Testing of Twist Actuated Single Cell Composite Beams for Helicopter Blade Control," M.S. Thesis, Massachusetts Inst. of Technology, Cambridge, MA, 1996.

[32] Tsushima, N., and Su, W., "Modeling of Highly Flexible Multifunctional Wings for Energy Harvesting," *Journal of Aircraft*, Vol. 53, No. 4, Feb. 2016, pp. 1033–1044. doi:10.2514/1.C033496

[33] Su, W., and Cesnik, C. E. S., "Strain-Based Geometrically Nonlinear Beam Formulation for Modeling Very Flexible Aircraft," *International Journal of Solids and Structures*, Vol. 48, Nos. 16–17, 2011, pp. 2349–2360. doi:10.1016/j.ijsolstr.2011.04.012

[34] Lewis, F. L., and Syrmos, V. L., *Optimal Control*, Wiley, New York, 1995, pp. 1–430.

[35] Lin, C.-F., *Advanced Control Systems Design*, Prentice–Hall, Upper Saddle River, NJ, 1993, pp. 1–128.

[36] Stefani, R. T., *Design of Feedback Control Systems*, Oxford Univ. Press, New York, 1993, pp. 675–709.

[37] Peters, D. A., and Johnson, M. J., "Finite-State Airloads for Deformable Airfoils on Fixed and Rotating Wings," *Symposium on Aeroelasticity and Fluid Structure Interaction Problems, ASME Winter Annual Meeting*, Vol. 44, American Soc. of Mechanical Engineers, New York, 1994, pp. 1–28.

[38] Jones, R. M., *Mechanics of Composite Materials*, McGraw–Hill, New York, 1975, pp. 55–467.

[39] Ortega-Morales, M., "Modeling and Control of the Aeroelastic Response of Highly Flexible Active Wings," Master's Thesis, Massachusetts Inst. of Technology, Cambridge, MA, 2000.